# Spectroscopic Studies of Inhibited Alcohol Dehydrogenase from *Thermoanaerobacter brockii*: Proposed Structure for the Catalytic Intermediate State[†]
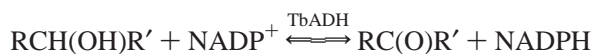
Oded Kleifeld,[‡] Anatoly Frenkel,[§,||] Oren Bogin,[⊥] Miriam Eisenstein,[@] Vlad Brumfeld,[@] Yigal Burstein,[⊥] and Irit Sagi*,[‡]

*Departments of Structural Biology and Organic Chemistry, The Weizmann Institute of Science, Rehovot 76100, Israel,
Department of Chemical Services, The Weizmann Institute of Science, Rehovot 76100, Israel, and
Materials Research Laboratory, University of Illinois at Urbana-Champaign, Urbana, Illinois 61801*

*Received February 1, 2000; Revised Manuscript Received April 7, 2000*

ABSTRACT: *Thermoanaerobacter brockii* alcohol dehydrogenase (TbADH) catalyzes the reversible oxidation of secondary alcohols to the corresponding ketones using $NADP^+$ as the cofactor. The active site of the enzyme contains a zinc ion that is tetrahedrally coordinated by four protein residues. The enzymatic reaction leads to the formation of a ternary enzyme–cofactor–substrate complex; and catalytic hydride ion transfer is believed to take place directly between the substrate and cofactor at the ternary complex. Although crystallographic data of TbADH and other alcohol dehydrogenases as well as their complexes are available, their mode of action remains to be determined. It is firmly established that the zinc ion is essential for catalysis. However, there is no clear agreement about the coordination environment of the metal ion and the competent reaction intermediates during catalysis. We used a combination of X-ray absorption, circular dichroism (CD), and fluorescence spectroscopy, together with structural analysis and modeling studies, to investigate the ternary complexes of TbADH that are bound to a transition-state analogue inhibitor. Our structural and spectroscopic studies indicated that the coordination sphere of the catalytic zinc site in TbADH undergoes conformational changes when it binds the inhibitor and forms a pentacoordinated complex at the zinc ion. These studies provide the first active site structure of bacterial ADH bound to a substrate analogue. Here, we suggest the active site structure of the central intermediate complex and, more specifically, propose the substrate-binding site in TbADH.

Alcohol dehydrogenases are involved in a wide range of metabolic functions. The interconversions of alcohols, aldehydes, and ketones are essential processes with both prokaryotes and eukaryotes. *Thermoanaerobacter brockii* alcohol dehydrogenase (TbADH)[1] is a medium-chain, $NADP^+$-linked (*1, 2*), class A enzyme (*3*) that reversibly catalyzes the oxidation of secondary alcohols to the corresponding ketones:

$$RCH(OH)R' + NADP^+ \overset{TbADH}{\rightleftharpoons} RC(O)R' + NADPH$$

Structurally, TbADH is a tetramer comprising four identical subunits, each containing 352 amino acid residues (molecular mass of 38 000 Da per subunit). The enzyme is stable at high temperatures [$t_{1/2}$ = 93.8 °C, a temperature at which 50% of the enzymatic activity is lost after 60 min (*4*)], tolerates organic solvents well, and exhibits broad specificity and high reactivity toward secondary alcohols, as well as low reactivity toward primary alcohols (*5–7*). The overall three-dimensional structures of TbADH and its analogous alcohol dehydrogenase from *Clostridium beijerinckii* (CbADH) have been studied by X-ray crystallography (*8*). The sequences of CbADH and TbADH are 75% identical, and they have very similar three-dimensional structures. Both are tetramers, and each protomer is composed of two domains: a cofactor-binding domain and a catalytic domain. These functional domains are separated by a deep cleft at the bottom, where a single zinc atom is bound in the catalytic sites. The crystal structures of TbADH and CbADH reveal

* To whom correspondence should be addressed: Department of Structural Biology, The Weizmann Institute of Science, P.O. Box 26, Rehovot 76100, Israel. Fax: 972-8-934 2130. E-mail: irit.sagi@weizmann.ac.il.
‡ Department of Structural Biology, The Weizmann Institute of Science.
§ University of Illinois at Urbana-Champaign.
|| Current address: Building 510E, Brookhaven National Laboratory, Upton, NY 11973.
⊥ Department of Organic Chemistry, The Weizmann Institute of Science.
@ Department of Chemical Services, The Weizmann Institute of Science.

that the single zinc ion in the catalytic site is bound to Cys 37, His 59, Asp 150, and Glu 60.

To elucidate the kinetic mechanism of catalysis, several research groups have investigated the steady-state kinetic mechanism of TbADH. Two main mechanisms have been proposed; both describe a sequentially ordered type reaction in which the cofactor (NADP$^+$ or NADPH) binds the free form of the enzyme, followed by the binding of the hydroxylate or ketonic substrate (9−11). However, several differences exist between these two proposed mechanisms. Ford et al. concluded that the kinetic mechanism is a sequential ordered bi-bi one, resulting in the formation of central ternary complexes (9). In contrast, Pereira et al. proposed a Theorell−Chance bi-bi mechanism in which the central ternary complexes are not substantially populated under steady-state turnover (11). In a recent report (10), Oestreicher et al. have extended these studies by performing product inhibition experiments and concluded that TbADH catalyzes the oxidation of secondary alcohols based on the Therole−Chance bi-bi kinetic model. Both proposed mechanisms include substrate binding and product release as central kinetic events of the mechanism.

X-ray crystallographic studies of TbADH in its holo form and CbADH in its apo and holo forms suggest that the mechanism of alcohol dehydrogenase catalysis may differ between bacterial alcohol dehydrogenases and the mammalian horse liver alcohol dehydrogenase (HLADH) (8). These observations are based mainly on the overall structure of both enzymes, the type of ligation around the catalytic zinc ion, and the lack of a structural zinc ion and a "proton relay" pathway in TbADH. The proton relay pathway, which was identified in HLADH, consists of a hydrogen bond network between key residues at the assigned catalytic pocket (12). It was proposed that the role of this proton relay system in HLADH is to transfer a proton from the substrate to the surface of the enzyme during the interconversion of primary alcohols.

To better understand the mode of action in bacterial alcohol dehydrogenase (ADH), we have compared the active site conformation of TbADH in various functional and inhibited complexes to those of HLADH complexes. We have studied TbADH complexed with its inhibitor dimethyl sulfoxide (DMSO) by X-ray absorption spectroscopy and have characterized it structurally. DMSO is considered to be an analogue of acetone, which is a substrate for TbADH and other ADHs, as demonstrated by kinetic models (13, 14). Consideration of DMSO as a substrate analogue rationalizes the specificity of its interaction with TbADH and provides a stable transition-state analogue complex that is suitable for accurate structural analysis (15). We used a combination of X-ray absorption, circular dichroism (CD), and fluorescence spectroscopy, together with structural analysis and modeling studies, to investigate the TbADH−NADP$^+$−DMSO and TbADH−NADPH−DMSO ternary complexes. Our structural and spectroscopic studies indicated that DMSO is bound to the catalytic zinc ion in TbADH. However, unlike HLADH (13), the coordination sphere of the catalytic zinc site in TbADH undergoes conformational changes when it binds the inhibitor and forms a pentacoordinated complex at the zinc ion. These studies provide the first active site structure of bacterial ADH that is bound to a substrate analogue. In this work, we suggest the active site structure of the central intermediate complex and, more specifically, propose the substrate-binding site in TbADH.

## MATERIALS AND METHODS

*Materials.* All chemicals that were used were of the highest purity and were obtained from Merck (Darmstadt, Germany), except when otherwise noted. Trisma base, PMSF, oxidized and reduced forms of β-nicotinamide adenine dinucleotide phosphate (NADP$^+$ and NADPH, respectively), D,L-dithiothreitol (DTT), ampicillin, and benzamidine were purchased from Sigma (St. Louis, MO). DEAE-Sepharose and Red Sepharose CL-6B were purchased from Pharmacia (Uppsala, Sweden). Ethylenediaminetetraacetic acid (EDTA) and 2-butanol were obtained from Fluka Chemical AG (Buchs, Swizerland). The protein assay kit was purchased from Bio-Rad Laboratories (Richmond, CA).

*Recombinant TbADH.* Recombinant TbADH was produced and purified to homogeneity in a three-step purification scheme as described by Peretz et al. (16) and Bogin et al. (17). The recombinant protein was obtained in good yield (about 300 mg/L) and with a specific activity of 65−70 units/ mg at 40 °C.

*Enzyme Assay.* The enzymatic activity of ADH was measured at 40 °C by following the absorption increase at 340 nm ($\epsilon_{340}$ = 6.2 mM$^{-1}$ cm$^{-1}$) for the formation of NADPH from NADP$^+$. The standard assay mixture contained 150 mM 2-butanol, 0.5 mM NADP$^+$, and 100 mM Tris-HCl (pH 9.0) in a total volume of 1 mL. One unit of ADH activity is defined as the amount of enzyme that catalyzes the formation of 1 $\mu$mol of NADPH per minute at the initial velocity under the previously mentioned conditions.

Enzymatic activity and kinetic parameters were measured and calculated using a Beckman DU-7500 spectrophotometer equipped with a Multicomponent/SCA/Kinetics Plus software package and a thermostatic water circulating bath.

*Kinetic Constants for the Inhibition Reaction of DMSO and TbADH.* DMSO inhibition was carried out with varied concentrations of 2-propanol (0.2−1.0 mM) and 0.5 mM NADP$^+$ in 100 mM Tris-HCl (pH 9.0) at 40 °C. The enzymatic activity of TbADH (final concentration of 30 nM) was measured, and the kinetic parameters were calculated for various concentrations of DMSO in the range of 0−30 mM.

*Inductively Coupled Plasma Atomic Emission Spectroscopy (ICP-AES).* The metal content in TbADH was analyzed by inductively coupled plasma atomic emission spectroscopy using an ICP-AES model "Spectroflame" from Spectro (Kleve, Germany). Zinc content was determined after extensive dialysis of protein samples (5 mg each), against three changes of 100-fold excess volumes of a solution of 25 mM Tris-HCl and 100 mM NaCl (pH 7.3). Samples were digested with nitric acid, and the volume was adjusted to 5 mL.

*Protein Concentration.* Protein concentrations were determined using a Bradford reagent with bovine serum albumin as a standard, and according to the analysis of amino acid composition.

*Circular Dichroism (CD).* CD was assessed using an Aviv spectrophotometer, model 202. The data were collected using quartz cells with a light path of 10 mm for near UV (250−320 nm) and 0.1 mm for far UV (180−240 nm). Samples

for the near UV scan contained 10 $\mu$M enzyme, 20 $\mu$M NADP$^+$, and 1 mM DMSO in 25 mM Tris-HCl buffer (pH 9.0). Samples for far UV scans contained 10 $\mu$M enzyme, 50 $\mu$M NADP$^+$, and 1 mM DMSO in 50 mM phosphate buffer (pH 8.0).

*Fluorescence Measurements.* Fluorescence was measured using a JASO 8100 fluorometer equipped with data processing software. The data were collected using quartz cells with a light path of 10 mm. Samples contained 1.5 $\mu$M enzyme, 20 $\mu$M NADP$^+$ (or NADPH), and 200 mM DMSO in 100 mM Tris-HCl buffer (pH 9.0).

*Structural Analysis and Modeling.* The crystal structures of HLADH, TbADH, and CbADH were analyzed using Insight II software from MSI. The model of the TbADH–NADP$^+$–DMSO complex was constructed on the basis of the experimental X-ray structures of TbADH (PDB entries 1PED and 1YKF) and the HLADH–DMSO complexes (PDB entry 6ADH). The DMSO molecule was manually docked into a pocket in the TbADH binding site, formed when the nicotinamide moiety in NADP$^+$ is rotated by its conformation in the HLADH–DMSO structure.

*X-ray Absorption (XAS). (1) Sample Preparation.* TbADH samples were extensively dialyzed against three changes of 100 volumes of 10 mM HEPES (pH 8.5). HEPES buffer was used to avoid drastic changes in pH at a cryogenic temperature. TbADH enzymatic activity was checked in HEPES buffer for all samples. After dialysis, the enzyme was concentrated by ultrafiltration using a Millipore Centricon-30 (Bedford, MA) apparatus to make a final concentration of 40 mg/mL. Samples were loaded into copper sample holders (10 mm $\times$ 5 mm $\times$ 0.5 mm) covered with Mylar tape and immediately frozen in liquid nitrogen. The frozen samples were then mounted into a Displex closed-cycle He cryostat, and their temperatures were maintained at 30 K, to minimize the thermal disorder in the XAS data.

*(2) Data Collection.* XAS data collection was performed at the National Synchrotron Light Source at Brookhaven National Laboratory (Upton, NY), beam line X9B. The spectra were recorded at the Zn K-edge in fluorescence geometry at a low temperature (30 K). The beam energy was defined using a flat Si (111) monochromator crystal. The incident beam intensity $I_0$ was recorded using an ionization chamber, and the fluorescence intensity was recorded using a 13-element Ge detector. The transmission signal from a zinc foil was measured with a reference ion chamber simultaneously with fluorescence for the purpose of beam energy calibration. Several scans of each sample were collected for a total of $1 \times 10^6$ counts across the edge. The samples were checked for burning marks after each scan, and the beam position on the sample was changed before each scan to minimize radiation damage. Enzyme activity was checked after exposure to X-rays, and the enzyme was found to be fully active.

*(3) Data Processing and Analysis.* The average Zn K-edge absorption coefficient $F(E)$ was obtained after several independent XAS measurements for each sample, which were aligned in absolute energy using the reference Zn metal foil XAS data as an absolute energy calibrant. Subsequently, the absorption coefficients for different samples were shifted in X-ray energy until their first inflection points were aligned at the same energy (9658 eV). This alignment assured, to a good approximation, that the same X-ray energy $E_0$ of 9658

eV could be chosen as the photoelectron energy origin in all data sets.

Smooth atomic background was removed with the AU-TOBK program of the UWXAFS data analysis package, developed at the University of Washington (Seattle, WA) (*18*). The same energy ($E_0 = 9658$ eV) was chosen for the purpose of background removal as the photoelectron energy origin. The $R$-space region for minimizing the signal below the first shell was chosen between 0 and 1 Å. After the background removal, the useful $k$-range in the resultant $k^2$-weighted $\chi(k)$ was between 2 and $10-11$ Å$^{-1}$. Model data for the fitting procedure were constructed by extracting out the catalytic zinc site coordinates (in a radius of 8 Å) from crystallographic coordinates of CbADH due to its higher resolution compared with that of the TbADH crystal structure (*19*). Using the computer code FEFF7 (*20*, *21*), we calculated the theoretical photoelectron scattering amplitudes and phase shifts. The total theoretical $\chi(k)$ was constructed by adding the most important partial $\chi(k)$ values that contributed to the $r$-range of interest.

The theoretical XAFS signal was fitted to the experimental data using the nonlinear least-squares method implemented in the program FEFFIT (*18*) in $R$-space, by Fourier transforming both the theory and data. Data and theory were weighted by $k$ and multiplied by a Hanning window function in Fourier transforms.

## RESULTS

We carried out a series of experiments using a combination of X-ray absorption spectroscopy (XAS), CD, and fluorescence spectroscopy, in addition to structural analysis and modeling studies, on native TbADH, the TbADH–NADP$^+$ complex, and the ternary inhibited complexes of TbADH, NADP$^+$ or NADPH, and DMSO. The zinc content and the quality of the protein were checked by examining the specific activity of the protein, ICP-AES, and gel electrophoresis assays before every experiment to ensure the optimal state of the protein during the experimental procedure. The TbADH samples contained 1 g of zinc/subunit, and their specific activity was $65-70$ units/mg at 40 °C.

*Inhibition of TbADH by DMSO.* DMSO is known to be a transition-state analogue inhibitor for ADHs (*15*, *22*). The relative activity of TbADH was measured after titration with DMSO. In this experiment, holo TbADH (TbADH and the cofactor) was incubated with the substrate 2-propanol and titrated with DMSO until complete inhibition was achieved. Effective inhibition of enzymatic activity was observed after adding 1 mM DMSO, and complete inhibition of the enzyme was reached with a total DMSO concentration of about 10 mM in the reaction mixture. The inhibition constant ($K_i$) obtained for TbADH inhibition by DMSO is $0.2 \pm 0.05$ mM. The kinetic parameters are consistent with the ones obtained by others for native TbADH and HLADH inhibition by DMSO (*10*, *11*, *22*).

*XAS Studies.* The local structures of the catalytic zinc ion in TbADH, holo TbADH (with NADP$^+$ and NADPH), and the inhibited TbADH–NADP$^+$–DMSO and TbADH–NADPH–DMSO complexes were studied by X-ray absorption near edge structure (XANES) and extended X-ray absorption fine structure (EXAFS) spectroscopy. EXAFS is a valuable technique for elucidating the structure of a variety
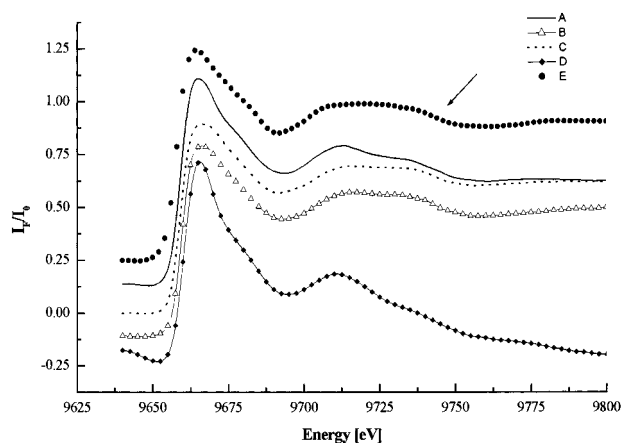
FIGURE 1: Raw XANES region data of TbADH complexes with cofactor and DMSO. Raw XAS data in the Zn K-edge region of TbADH (—, A), TbADH−NADP$^+$ (△, B), TbADH−NADPH (···, C), TbADH−DMSO−NADP$^+$ (◆, D), and TbADH−DMSO−NADPH (○, E). All data sets were normalized by fitting a linear polynomial function from −150 to −20 eV and from 75 to 200 eV below and above the edge, respectively. The edge step was determined by the difference between the pre-edge and post-edge fits. The overall shape of the edge spectra of each sample differs. The most distinct features are the edge position, the edge shape, and changes of the ~9730 eV peak at the XANES region (marked with an arrow). Such an alternation in edge structure indicates that TBADH undergoes conformational changes at the catalytic zinc ion upon binding of cofactors and the transition-state analogue inhibitor DMSO.

of metal sites in metalloproteins (*23−29*). More specifically, the technique measures the transition from the core electronic states of the metal to the excited electronic or continuum states. XAS studies can be conducted in any state of matter, for example, gas, liquid, or crystalline phases. Spectral analysis near the electronic transition (XANES) provides information about the metal's charge state and its geometry. Spectral analysis above the absorption edge, in the EXAFS region, provides complementary structural information such as coordination numbers, types, and distances from neighboring atoms to the central (absorbing) atom. In addition, XAS is an excellent structural tool for probing the d$^{10}$ zinc ion, which is generally spectroscopically silent.

In light of this, we conducted XAS studies to examine the nature and bonding of active site ligands and the changes in metal site structures upon binding of DMSO to TbADH. Figure 1 shows normalized absorption edge data of native TbADH compared with its spectra when bound to NADP$^+$ and NADPH, and in its ternary complexes when bound to NADP$^+$ and DMSO, and NADPH and DMSO. Remarkably, the edge spectra in Figure 1 show substantial changes at the edge position and in the XANES region between native TbADH and its various complexes. The Zn absorption edge shifts to higher energy upon the addition of both cofactors. Interestingly, the edge position is further shifted to a higher energy upon binding to NADP$^+$ and DMSO, which is shifted back toward a lower edge energy, relative to native TbADH, when it is bound to NADPH and DMSO. Substantial shifts in energy are directly correlated with changes in the charge distribution around the metal ion and may also indicate a change in the coordination number. These changes in different chemical environments can alter the core-level binding energies and consequently produce absorption edge shifts that show up in the XANES (*30*). The 1.5 eV edge

shift to a higher energy, which is observed upon the binding of DMSO to holo TbADH, is consistent with an increase in the oxidation state of the metal ion, as reported by Wirt et al. (*31*). Alternations in the charge distribution of the zinc ion in the various complexes indicate that the zinc ion has a catalytic role and is central to catalysis.

Changes in the spectral features of XANES are observed in all complexes at 9663−9735 eV (Figure 1). We have, therefore, assigned these consistent changes in the various complexes to the local changes at the coordination sphere of the catalytic zinc site in TbADH, when it binds the transition-state analogue inhibitor. In addition, the relatively small reduction in peak intensity observed at 9735 eV in the TbADH−NADP$^+$ complex indicates that moderate conformational changes occur at the catalytic pocket upon cofactor binding, as reported previously in crystallographic studies (*19*).

The results of the EXAFS data analysis of TbADH, TbADH−NADP$^+$, and TbADH−NADP$^+$−DMSO and −NADPH−DMSO complement our edge analysis. Table 1 and Figure 2 present the fitting results of the catalytic zinc site of TbADH and complexes.

Standard and simultaneous curve-fitting procedures were used to fit the FEFF7 theory data (*20*) to the real and imaginary parts of the Fourier-transformed $\chi(k)$. The $k^2$ weighting factor and the Hanning window function, defined between 2 and 10 Å$^{-1}$ for the TbADH, TbADH−NADP$^+$, and TbADH−NADPH data, and between 2 and 11 Å$^{-1}$ for the inhibited complexes data, were used in Fourier transforms. During the fitting procedure, the corrections to the energy origin ($\Delta E_0$), bond distances ($\Delta R$), and mean square disorders of the distances ($\sigma^2$) were varied until the best fit was obtained. The number of relevant independent data points $N_{idp}$ in the data was calculated using eq 1 (*32*)

$$N_{idp} = \frac{2\Delta k \Delta r}{\pi} + 2 \qquad (1)$$

where $\Delta k$ and $\Delta r$ represent the data ranges in $k$ and $r$ spaces, respectively. Equation 1 implies that the number of fit variables $P$ should be smaller than $N_{idp}$. To reduce the number of fit variables, we fixed the many-body factor $S_0^2$ at 1.0, and the following fitting procedures were developed.

The same theoretical single-scattering paths corresponding to the first shell Zn−N, Zn−O1, Zn−O2, and Zn−S distances were fit to all data sets simultaneously (Zn−O1 and −O2 represent different Zn−O ligands in the model). The $\Delta r$ fitting range was from 1 to 2.1 Å, which corresponds to the first shell. The following constraints were applied to the different fitting parameters. All $\Delta E_0$ corrections were constrained to be identical for all paths and for all data sets. This approximation is justified because the raw absorption coefficients are aligned in energy as previously described. The corrections $\Delta R$ to the model Zn−O1 and Zn−O2 distances were constrained to be the same, since these bond lengths are proximal to each other in the model. In addition, the mean square disorders in the Zn−N bond lengths for all these complexes ($\sigma^2$) were constrained to be equal to each other, as were those for the Zn−O and Zn−S bond distances. This is a reasonable approximation, since these bond force constants are not expected to be too different between the same atomic pairs in the various complexes, where the

Table 1: EXAFS Curve-Fitting Results

| | $A^a$ | | |
| --- | --- | --- | --- |
| | TBADH | TBADH$-$NADP$^+$ | TBAD$-$NADP$^+-$DMSO |
| $\Delta E_0$ (eV) | $-2.7$ (2.6) (V) | $-2.7$ (2.6) (C) | $-2.7$ (2.6) (C) |
| $N$, ZN$-$O | 2 (F) | 2 (F) | 2.61(68) (V) |
| $R$, ZN$-$N (Å) | 1.82(6) (V) | 1.81(7) (V) | 1.78(10) (V) |
| $R$, ZN$-$O1 (Å) | 1.95(4) (V) | 1.94(4) (V) | 1.93(4) $\times$ 2 (V) |
| $R$, ZN$-$O2 (Å) | 1.97(4) (C) | 1.96(4) (C) | 1.96(4) (C) |
| $R$, ZN$-$S (Å) | 2.24(2) (V) | 2.21(3) (V) | 2.31(2) (V) |
| $\sigma^2$, ZN$-$N (Å$^2$) | 0.0000(33) (V) | 0.0000(33) (C) | 0.0000(33) (C) |
| $\sigma^2$, ZN$-$O (Å$^2$) | 0.0000(33) (C) | 0.0000(33) (C) | 0.0000(33) (C) |
| $\sigma^2$, ZN$-$S (Å$^2$) | 0.0000(22) (V) | 0.0000(22) (C) | 0.0000(22) (C) |

| | $B^b$ | | | | | |
| --- | --- | --- | --- | --- | --- | --- |
| | TbADH | TbADH$-$NADP$^+$ | TbADH$-$NADPH | TbADH$-$NADP$^+-$DMSO$^c$ | TbADH$-$NADP$^+-$DMSO$^d$ | TbADH$-$NADPH$-$DMSO |
| $\Delta E_0$ (eV) | 0 [C] | 0 [C] | 0 [C] | $-2.7$ [C] | 0 [C] | 3.0 [C] |
| $R$, Zn$-$N (Å) | 1.81(3) [V] | 1.83(4) [V] | 1.80(5) [V] | 1.83(1) [C] | 1.83(2) [V] | 1.87(1) [V] |
| $R$, Zn$-$O1 (Å) | 1.98(2) [V] | 1.96(3) [V] | 1.99(3) [V] | 1.85(1) [C] | 1.83(3) [V] | 1.75(1) (V) |
| $R$, Zn$-$O2 (Å) | 2.01(2) [V] | 1.98(3) [V] | 1.99(3) [C] | 2.02(2) $\times$ 2 [C] | 2.00(2) [V] | 2.01(1) [C] |
| $R$, Zn$-$O3 (Å) | $-$ | $-$ | $-$ | $-$ | 2.10(3) [V] | 2.05(1) [V] |
| $R$, Zn$-$S (Å) | 2.24(2) [V] | 2.21(3) [V] | 2.24(3) [V] | 2.24(2) [V] | 2.25(3) [C] | 2.25(1) [C] |
| $\sigma^2$, Zn$-$N (Å$^2$) | $1.6 \times 10^{-5}$ [V] | $8.3 \times 10^{-4}$ [V] | $2.4 \times 10^{-3}$ [V] | $1.1 \times 10^{-3}$ [V] | $1.0 \times 10^{-4}$ [V] | $1.0 \times 10^{-6}$ [C] |
| $\sigma^2$, Zn$-$O1 (Å$^2$) | $3.5 \times 10^{-3}$ [V] | $3.0 \times 10^{-5}$ [V] | $4.6 \times 10^{-3}$ [V] | $1.1 \times 10^{-3}$ [C] | $1.0 \times 10^{-4}$ [V] | $5.0 \times 10^{-4}$ [C] |
| $\sigma^2$, Zn$-$O2 (Å$^2$) | $3.5 \times 10^{-3}$ [V] | $3.0 \times 10^{-5}$ [V] | $4.6 \times 10^{-3}$ [C] | $1.1 \times 10^{-3}$ [C] | $1.0 \times 10^{-4}$ [V] | $1.0 \times 10^{-6}$ [V] |
| $\sigma^2$, Zn$-$O3 (Å$^2$) | $-$ | $-$ | $-$ | $-$ | $1.0 \times 10^{-4}$ [V] | $1.0 \times 10^{-6}$ [V] |
| $\sigma^2$, Zn$-$S (Å$^2$) | $1.2 \times 10^{-5}$ [V] | $1.1 \times 10^{-4}$ [V] | $2.8 \times 10^{-5}$ [V] | $1.2 \times 10^{-3}$ [V] | $1.0 \times 10^{-4}$ [C] | $1.0 \times 10^{-5}$ [V] |

$^a$ Results of simultaneous EXAFS curve-fitting analysis for TbADH, the TbADH$-$NADP$^+$ complex, and the TbADH$-$NADP$^+-$DMSO complex. The uncertainties are given in parentheses. The symbols F, V, and C stand for fixed, varied, and constrained, respectively, and indicate how the respective parameter was treated in the fit, as described in the text. Zn$-$O1 and Zn$-$O2 represent the different Zn$-$O distances in the model. $^b$ Results of EXAFS curve-fitting analysis after the simultaneous fit was refined (part A). Part B lists the best fitting results that were obtained for the various complexes of TbADH. The ternary-inhibited complex is consistent with three Zn$-$O bond distances, one Zn$-$N bond distance, and one Zn$-$S bond distance. Zn$-$O1, Zn$-$O2, and Zn$-$O3 represent the different Zn$-$O ligands in the model. $^c$ The native TbADH that was constructed from crystallographic data was used in the fitting procedure. $^d$ The ternary-inhibited model that was constructed from our modeling studies was used in the fitting (see Results). The estimated error on the total number of the Zn$-$O ligands is $\pm 0.5$. The coordination number at the catalytic zinc ion is consistent with five or six ligands.

nearest atomic environment is similar. The number of variables was further decreased by constraining the $\sigma^2$ to be identical for all Zn$-$N and Zn$-$O bonds. Therefore, the total number of variables was 13: $\Delta E_0$ and $N$ for the Zn$-$O1 bond in DMSO; $\Delta R$ for three Zn$-$N, three Zn$-$O1, and three Zn$-$S bonds; and $\sigma^2$ for the Zn$-$N and Zn$-$S bonds. The number of independent points was 20. The possibility of having more than two nearest-neighbor oxygen ligands in the TBAD$-$NADP$^+-$DMSO complex was accounted for by varying the number $N$ of O1s in the data set, which results in a stable minimum at $2.7 \pm 0.7$ ligands. Table 1A presents the results of the simultaneous fitting procedure. The Zn$-$N (His) bond distances appear to be shortest at about 1.8 Å in all complexes. The Zn$-$O distances are similar in all the fits except for the additional contribution of oxygen in the ternary complex. The Zn$-$S bond appears to be longer (2.31 Å) in the inhibited complex; however, further analysis showed that this distance might be overestimated due to correlation problems in the fit.

The simultaneous multiple-data set fitting procedures provided us with the basic fitting parameters to be used for the final refinement of the local structures in all five complexes. Distance and coordination number parameters obtained by the multiple-data set analysis for each complex were refined by analyzing each data set separately, avoiding the use of heavy constraints. This procedure yielded better $\chi^2$ and r-factors for all fits. The possibility of a higher coordination number (more than four ligands) at the active zinc site of TbADH$-$NADP$^+-$DMSO and TbADH$-$

NADPH$-$DMSO complexes was further examined by stepping the coordination number and $\Delta E_0$ in a standard curve-fitting analysis. Each data set (for each complex) was fitted separately by a theoretical model, which included the first- and second-shell contributions using a standard EXAFS analysis procedure. To examine the stability of the fitting results at the minimum, we increased the number of the oxygen ligands in the fit from two to five and stepped it up in increments of one ligand at a time. For example, in the fitting analysis of the TbADH$-$NADP$^+-$DMSO complex, such a procedure gave $R$-factors of 0.019, 0.007, 0.0071, and 0.0075. The reduced $\chi^2$ behaved similarly, being higher (not acceptable) for the five-oxygen fit. These results were consistent with three or four Zn$-$O ligand contributions, one Zn$-$N contribution, and one Zn$-$S contribution at the catalytic site of the inhibited complex of TbADH.

Comparison of the Zn coordination in TbADH and TbADH$-$NADP$^+$ has confirmed the crystal structure, revealing a tetrahedral structure around the zinc ion in both complexes. The distances around the metal ion, obtained by XAS curve-fitting analysis, do not exhibit significant changes upon binding of the cofactor. Moreover, distance and coordination number parameters in the various complexes manifest the same trend that was obtained in the simultaneous fits. The distances in the catalytic zinc site in the TbADH$-$NADP$^+-$DMSO ternary complex are 1.83 Å for one Zn$-$N bond, 2.24 Å for one Zn$-$S bond, 1.85 Å for one Zn$-$O bond, and an average of 2.05 Å for two or three Zn$-$O ligands. The zinc site coordination in the TbADH$-$NADPH$-$
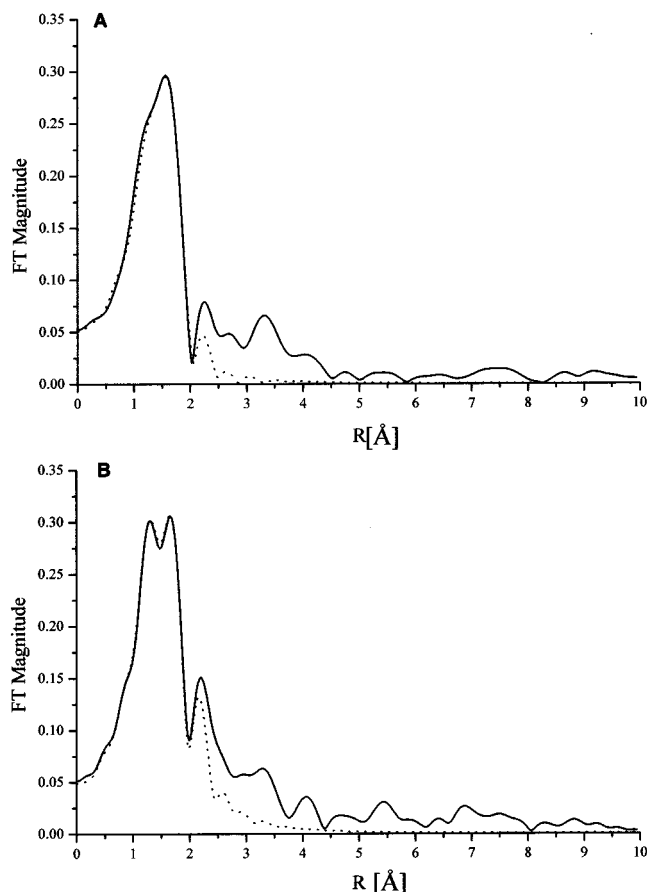
FIGURE 2: EXAFS fitting results of the zinc site in the native TbADH and the TbADH−NADP⁺−DMSO complex. Representation of fitting results in *R*-space of experimental data (—) of native TbADH (A) and TbADH−NADP⁺−DMSO (B) to simulated theoretical Zn−ligand contributions of the TBADH active site (· · ·). Experimental data were extracted and normalized using the UWXAFS analysis package. The theoretical XAFS signal was constructed of apo-CBADH subunit B active site data (PDB entry 1PED) and calculated using FEFF7. The experimental data were fitted to the theoretical data using the nonlinear least-squares method implemented in the program FEFFIT in *R*-space, by Fourier transforming both theory and data. Data and theory were weighted by *k* and multiplied by a Hanning window function (with margins of 2 Å⁻¹) for the Fourier transforms. The fits shown here were preformed using an *R*-window from 1 to 2.1 for both samples and in a *k*-window from 2 to 10 for the native form (A) and from 2 to 10.5 for the ternary complex form (B).

DMSO complex is consistent with bond distances of 1.87 Å for one Zn−N bond, 2.25 Å for one Zn−S bond, 1.74 Å for one Zn−O bond, and an average of 2.03 Å for two or three Zn−O ligands.

In addition, the TbADH−NADP⁺−DMSO and −NADPH−DMSO XAS data were fitted to a new theoretical model of the active site, which was constructed from our studies of structural analysis (see Figure 5). Specifically, the new model contained a DMSO molecule directly bound to the zinc ion in the catalytic site of TbADH. Initial fits were performed by varying the coordination number of the three Zn−O contributions, which represent the Zn−Glu, Zn−Asp, and Zn−DMSO bonds. The best fit was obtained with three or four Zn−O ligands, which is consistent with the total of five or six ligands around the zinc ion. First-shell parameters were determined by varying $\Delta R$ and $\sigma^2$ for all first-shell paths (Table 1). To further examine the validity of these results,
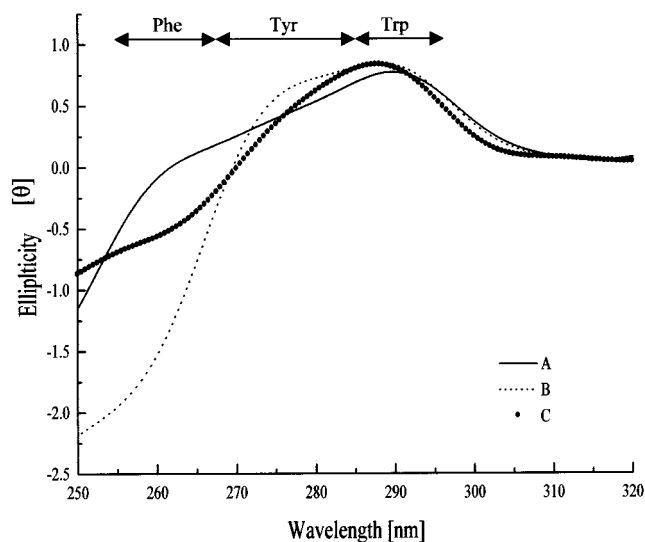


FIGURE 3: Near UV CD spectra of TBADH, TBADH−NADP⁺, and TBADH−NADP⁺−DMSO. Near UV CD spectra between 250 and 320 nm of TBADH (A), the TBADH−NADP⁺ complex (B), and the TBADH−DMSO−NADP⁺ complex (C) were measured at 25 °C after excitation at 280 (a) and 295 nm (b). Spectra were obtained by subtracting the background spectra relevant to each sample (same sample components without TBADH) and normalizing the data to the signal at 315 nm. The regions of contribution of aromatic amino acids are denoted.
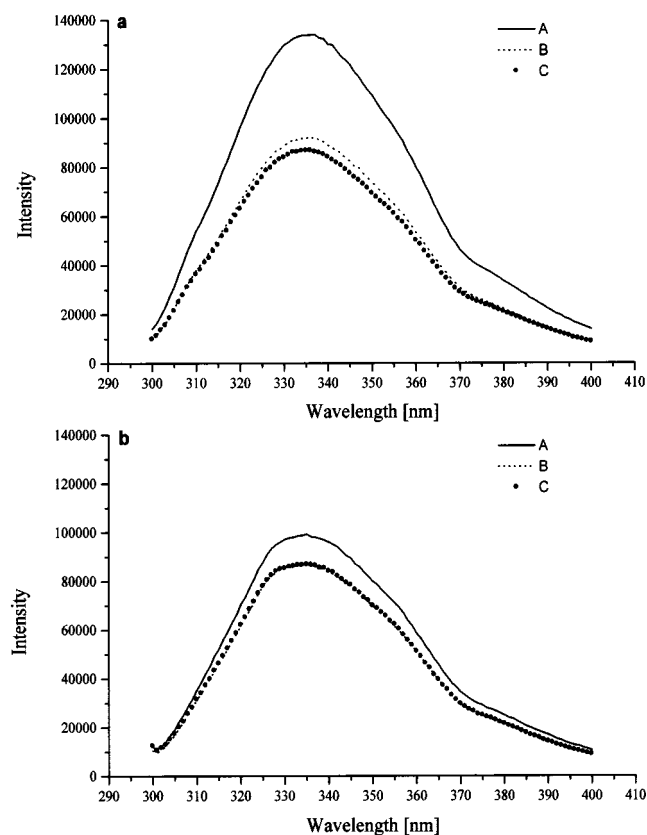


FIGURE 4: Fluorescence spectra of native TBADH, TBADH−NADP⁺, and TBADH−NADP⁺−DMSO. Fluorescence emission spectra between 300 and 400 nm of native TBADH (A), the TBADH−NADP⁺ complex (B), and the TBADH−NADP⁺−DMSO complex (C) were measured at 25 °C.

we fit the data to a single Zn−O contribution with a varying coordination number while constraining most of the other parameters. The number of Zn−O contributions obtained by
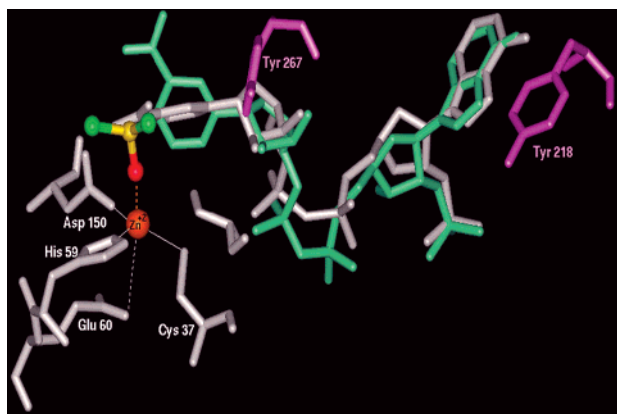
FIGURE 5: Active site modeling representation of the TbADH—NADP$^+$—DMSO complex. Superimposition of the structures of the TbADH—NADP$^+$ and TbADH—NADP$^+$—DMSO complexes reveals the conformation changes that take place upon binding of DMSO. A substantial structural change at the active site is observed at the nicotinamide ring with respect to the rest of the NADP$^+$ molecule. Rotation of the ring (light green) allows DMSO to bind to the zinc ion in the catalytic site in TbADH. This rotation allows the accommodation of the DMSO oxygen (red) as a fifth ligand at the catalytic zinc ion. The changes at the active site upon NADP$^+$ and DMSO binding are accompanied by changes in the conformation and the environment of Tyr 267, and to a lesser extent at Tyr 218 (purple). The DMSO molecule is sandwiched between the aromatic rings of nicotinamide and Trp 110 (not shown). This structural representation of the ternary-inhibited complex suggests a pentacoordination intermediate state of TbADH during catalysis.

this procedure was 3.8 ± 0.9, and the average distance was 2.02 Å. Repeating this procedure with fixing of one Zn—O contribution resulted in a coordination number of 2 ± 0.2 (to yield a total of three Zn—O contributions) and an average distance of 2.06 Å. Although these fits resulted in high Debye—Waller factor values because of the fit constraints and the distorted zinc site, they provide additional support for the pentacoordinate zinc site in TbADH—NADP$^+$—DMSO and —NADPH—DMSO complexes.

The metal—ligand distances at the catalytic site, which were derived from the crystal structure of holo TbADH, are 2.07 Å for the Zn—O(Asp) bond, 3.8 Å for the Zn—O(Glu) bond, 1.95 Å for the Zn—N(His) bond, and 2.33 Å for the Zn—S(Cys) bond. A survey of Zn(II)—N and —O bond distances within the metallo-organic complexes (taken from the Cambridge data bank) revealed Zn—N and Zn—O distance ranges of 1.90—2.04 and 1.80—2.05 Å, respectively, for tetrahedral complexes and 1.9—2.15 and 1.8—2.25 Å for pentacoordination complexes, respectively. A similar survey for Zn—S distances (taken from the Protein Data Bank and the Cambridge data bank) reported distances in a range of 2.23—2.36 Å. The distances obtained from our curve-fitting procedures are in good agreement with these results and therefore provide refined local structures of the zinc coordination at the catalytic sites of the native enzyme and holoenzyme of bacterial alcohol dehydrogenase complexes.

The Fourier-transformed (FT) EXAFS data of the ternary-inhibited complexes resulted in a distinct split in the first-shell peak of the FT spectrum (Figure 2B). The shape of the FT peak (in the ternary complexes) was maintained throughout a series of background removal conditions and appeared only in the ternary complex. A combination of two distinct peaks in the FT first shell suggests a distance distribution of

bond lengths, which is supported by our fitting results (Table 1).

Our XAS analysis described here is consistent with a coordination number of five or six at the catalytic zinc ion in TbADH. Attempts to fit the data to the tetracoordination sphere failed or resulted in unreasonable Debye—Waller factor values. Figure 2 shows the fitting results in *R*-space of native TbADH and the TbADH—NADP$^+$—DMSO complex. Table 1 lists the fitting results and parameters for the various complexes. Best fits were obtained by introducing the second-shell contributions in the fitting procedure. Standard errors associated with EXAFS-derived distances are ±0.03.

To further investigate the inhibitory effect of DMSO on TbADH in solution, we conducted UV CD and fluorescence studies. UV CD experiments were conducted with both NADP$^+$ and NADPH as cofactors and revealed the same spectral trend. Fluorescence experiments were conducted with NADP$^+$ following protein fluorescence studies.

*UV CD Studies.* Most of the UV CD measurements were conducted with NADP$^+$ as a cofactor because of chemical stability of NADPH. Figure 3 shows the near UV CD spectra of native TbADH, TbADH—NADP$^+$, and TbADH—NADP$^+$—DMSO. Changes in near UV CD spectra can serve as footprints for changes in the ternary structures of aromatic residues in specific wavelengths (*33, 34*). Typical transitions at 285—298, 265—283, and 255—265 nm are assigned for the aromatic residues tryptophan, tyrosine, and phenylalanine, respectively. Figure 3 shows that two peaks are changed upon addition of the cofactor. A large change in peak intensity (going to a negative value) is observed at 259 nm, probably due to the aromatic adenine ring of the cofactor. The change at 275 nm can be assigned to the 120° rotation of Tyr 218 due to cofactor binding, as indicated by crystallography (*8*). The tryptophan region at 289 nm is stable and resistant to changes in all spectra. No change was observed in the TbADH and TbADH—DMSO spectra (data are not shown).

Inhibition of TbADH with DMSO results in a substantial change in the peak at 266 nm. We assigned this change mainly to the exposure of Tyr 267 to solution upon the binding of DMSO to the zinc ion, as indicated by our modeling results. The change in peak intensity at 266 nm can also be partly accounted for by the further rotation of Tyr 218, due to changes in the cofactor position upon binding to DMSO. These results clearly show that some aromatic residues, presumably located at the active site of TbADH, reorganize their position upon cofactor and inhibitor binding. A comparison of the overall shape of the UV CD signal of the ternary-inhibited complex with native TbADH suggests that the binding of DMSO retained the native conformation of the catalytic site. This may indicate that the catalytic site in the productive enzyme is large enough to accommodate the DMSO molecule at the catalytic site, as indicated by XAS.

Far UV CD studies (*35, 36*) (data not shown) indicate that there is no conformational change in the secondary or tertiary structure of TbADH upon the addition of NADP$^+$ and DMSO. These results are consistent with the crystal structures of TbADH (*8*). In contrast to HLADH, no conformational changes upon cofactor binding were observed in TbADH.

*Fluorescence.* Inhibition by DMSO was also investigated by fluorescence spectroscopy. We measured the emission spectra of the protein in various complexes after excitation at 280 and 295 nm (Figure 4). Binding NADP$^+$ to TbADH resulted in substantial quenching of the fluorescence signal and was observed in both spectra. Adding DMSO to TbADH−NADP$^+$ caused further moderate quenching observed only after excitation at 280 nm.

Emission after excitation at 280 nm reflects the contribution of tryptophans and energy transfer from tyrosines to tryptophans, whereas emission after excitation at 295 nm reflects only changes in the contribution of tryptophan (*37*). Our results indicate that the quenching induced by NADP$^+$ and DMSO occurs mainly at the tyrosine residue level. These results are consistent with our near UV CD spectra and again confirm our experimental results, which are described here. The addition of NADPH to TbADH in the absence and presence of DMSO results in a similar fluorescence pattern. Interestingly, the quenching induced by NADPH and DMSO involves both tyrosines and tryptophans (data are shown). Although, the reaction conditions used in this assay were not optimal for the binding of NADPH (pH 9.0), this may suggest that DMSO binds to the TbADH−NADPH complex near tryptophan residues, as is also suggested by our modeling analysis.

*Structural Analysis and Modeling Studies.* Characterization of the conformational changes that take place at the active site of TbADH during substrate or inhibitor binding is necessary for understanding the enzymatic catalysis occurring in TbADH. To this end, we superimposed the structures of TbADH and HLADH and constructed a model structure of the TbADH−NADP$^+$−DMSO complex.

The apo and holo crystal structures of CbADH, which are closely related to TbADH, were compared. Superimposition of both structures indicates that the largest changes in conformation that occur in the active site upon cofactor binding consist of the rotation of the side chains of Tyr 267, Tyr 218, Met 285, Arg 200, and His 42 along with small backbone and side chain conformational changes for Lys 340. A comparison of the holo structures of CbADH and TbADH shows that the conformations of Tyr 267 and Tyr 218 in the two structures are similar. The binding of NADP$^+$ affects mostly the conformation of Tyr 267 and, to a lesser extent, Tyr 218, which are located near the catalytic site of the enzyme in TbADH. Superposition of the structures of HLADH and HLADH−NAD−DMSO reveals that the major structural change at the active site is the rotation of the nicotinamide ring with respect to the rest of the NADP$^+$ molecule. As shown in Figure 5, this rotation enables the DMSO molecule to bind the zinc ion at the catalytic site in TbADH. Interestingly, the zinc ion in TbADH does not need to rearrange its coordination sphere substantially upon DMSO binding. Thus, in contrast to the catalytic zinc ion in the HLADH−NAD−DMSO complex, which exhibits tetrahedral coordination (*38, 39*), in TbADH the tetrahedron is severely distorted and three out of the four ligands are almost coplanar. Such a configuration allows the accommodation of a fifth ligand at the zinc ion, creating a bipyramidal geometry. When a DMSO molecule is placed in this position, it is sandwiched between the aromatic rings of the nicotinamide and Trp 110. The most significant conformational change required for binding DMSO is therefore the rotation

of the cofactor nicotinamide ring, as observed in HLADH and as shown in our fluorescence and CD results (see Figures 3 and 4).

## DISCUSSION

Different catalytic mechanisms for alcohol dehydrogenase (ADH) have been proposed for catalysis on the basis of accumulating structural and spectroscopic evidence gathered from the most studied enzyme, HLADH (*1, 2*). It is now agreed that catalysis involves (1) different ligand states of the active site zinc ion during the catalytic cycle, (2) conformational changes of the protein induced by cofactor binding, and (3) temporal separation of proton abstraction from the chemical step of hydride transfer. These molecular events are controlled by ionizing groups for which a specific assignment remains controversial, despite the availability of numerous structural, chemical, and kinetic studies. The two main types of structural mechanisms that have been proposed for HLADH differ specifically in the hypothesized coordination of the zinc ion during catalysis. In both mechanisms, however, the role of the coordinated water molecule in HLADH seems to be important for catalysis. This bound water molecule and the proton charge relay, created by a hydrogen bond system at the catalytic site, as suggested by Branden et al. (*40*), perform an acid−base catalysis in the reaction. On the basis of a proton relay system, it was proposed by Dworschack and Plapp (*41*) that the alcohol molecule is added to the tetrahedral zinc ion to form pentacoordinated zinc during catalysis. In contrast, Dunn et al. and other researchers (*42−44*) also proposed a mechanism based on a charge relay system whereby the substrate displaces the zinc-bound water without going through a pentacoordinated intermediate. To date, there is no clear agreement about the coordination number around the metal ion or the ionization states of the metal-bound substrate during the course of catalysis in alcohol dehydrogenase systems.

An interesting development in the field occurred when the crystal structures of the mesophilic and thermophilic forms of bacterial ADH became available (*19*). The structure of the active site in the bacterial ADH was found to be different from that of the mammalian ADH. The differences are mainly due to the type of first-shell ligation around the catalytic zinc ion and the absence of a hydrogen bonding network that forms the charge relay system in HLADH. On the basis of the crystal structures, it was concluded that the mechanism of catalysis in bacterial ADHs and HLADH might differ. The exact location of the substrate has not been identified by crystallography, adding to this inconclusiveness. A first attempt to cocrystallize TbADH with substrate was recently reported by Shoham and colleagues (*45*). However, this structure represents only a binary complex with TbADH and 2-butanol as a substrate. The authors suggest a mechanism in which the zinc ion is displaced to its catalytic position after cofactor binding. This hypothesis is interesting; however, our structural studies on native, functional, and nonfunctional complexes failed to reveal any of these changes on the zinc ion. In addition, we speculate that such a rearrangement should be favorable by energetic and thermodynamic considerations at the active site of TbADH.

Changes in the charge distribution on the zinc ion in the various complexes (Figure 1) suggest that the metal ion is

required for chemical stabilization of the various intermediate states during catalysis. The structural similarity between the TbADH−NADP⁺−DMSO and TbADH−NADPH−DMSO complexes, revealed by our XAS analysis, suggest that substrate binding and product release are mediated by a central event at the zinc ion. This hypothesis is consistent with the kinetic models suggested for TbADH (*9−11*).

Furthermore, our experimental and modeling studies on the ternary TbADH−inhibitor complex suggest that the substrate site can be sandwiched between the cofactor and the Trp 110 side chain, while binding the zinc ion (Figure 5). This configuration is analogous to the one observed in HLADH. Recent studies by Colby et al. (*46*) have demonstrated, by double mutation and crystallography of ternary complexes, that the substrate and the cofactor in HLADH have to be sufficiently close. In this way, this conformation will allow a direct transfer of a hydride ion from the alcohol secondary carbon to the C4 position of the nicotinamide ring. In addition, the contribution of quantum mechanical tunneling to this hydride transfer step has been demonstrated (*47*).

The reaction conditions of TbADH and complexes taken in our measurements were chosen on the basis of maximum enzyme activity detected at a given pH and under specific salt conditions. The catalytic activity of liver alcohol dehydrogenase is strongly pH-dependent over a wide range. It has been established that this pH dependence is derived from the combined effects of pH on several steps in the catalytic mechanism. The dissociation of the HLADH−NAD⁺ and HLADH−NADH complexes exhibits pronounced pH dependence, which is not present for the dissociation of the zinc-free enzyme−cofactor complex (*48*). It is widely believed that the zinc-bound water molecule is linked to a proton relay system in the horse liver enzyme, since it allows the proximity of the nicotinamide ring in the binary enzyme, which probably accounts for the strong $pK_a$ dependence.

Our structural analysis and modeling studies suggest that a conformation change occurs in the active site of related tyrosine residues (Tyr 267 and Tyr 218) and an approximately 90° rotation of the nicotinamide ring occurs upon cofactor and DMSO binding. In our model, the DMSO molecule is in direct contact with the nicotinamide group of the cofactor. Our model is supported by our CD and fluorescence spectroscopy results (Figures 3 and 4), which show a relatively large rearrangement of aromatic residues upon binding of NADP⁺ and a more subtle change after the binding of DMSO.

Recent Raman spectroscopy studies by Deng et al. on inhibited HLADH suggest an energetic transition-state model for the ternary HLADH complex, where the zinc is bound in a tetraheadral coordination and the inhibitor molecule is linked to Ser 48 through a hydrogen bond (*49*). Similarly, we measured the distance between the DMSO ligand and the analogous residue Ser 37 in our model for the inhibited TbADH. The distance between the residues is 3.1 Å, which is within hydrogen bond distance, given the limited accuracy of model structures.

The possibility of a different mechanism of action in bacterial ADH was initially proposed by Korkhin et al., on the basis of the bacterial ADH crystal structures (*19*). This proposal took into consideration the general protein structure as well as the type of ligation around the catalytic zinc ion. The likelihood of zinc-bound His, Asp, Glu, and Cys residues

occurring in secondary structural elements has been calculated for catalytic and structural zinc in protein structures (*50, 51*). Because of the large propensity (65%) that was irrespective of its functional or structural role, it was suggested that the zinc ligation does not impose any extra constraints on secondary structures. In addition, it was demonstrated that in 8% of the cases, mostly in carbonic anhydrases, the zinc ion in protein−inhibitor complexes exhibited pentacovalant coordination. Moreover, most (74%) of the pentacoordinated catalytic zinc ions have trigonal bipyramid geometries (*50, 51*).

On the basis of our studies and the results with X-ray crystallography of TbADH previously reported (*19*), we propose that the mechanism of action in bacterial alcohol dehydrogenases is different from that of mammalian alcohol dehydrogenase, and that it has a pentacoordinated $Zn^{2+}$ intermediate. The structural differences between HLADH and TbADH are reflected by the lack of any significant change in the far UV CD studies of TbADH upon cofactor binding and in the different architecture of the catalytic metal site. Our XAS data analysis is consistent with a coordination number of five or six at the catalytic zinc ion in TbADH−NADP⁺−DMSO and −NADPH−DMSO complexes. The average expansion in the first-shell distances, from the native enzyme to the ternary complex, supports a higher coordination number at the zinc ion. Our modeling studies suggest a pentacovalent coordination number with a trigonal bipyramidal conformation in the central intermediate complex during catalysis. However, we cannot rule out the possibility of a sixth ligation by oxygen from a proximal amino acid residue.

At this stage, our results support the presence of a proton relay system that facilitates catalysis. However, further investigations are needed to prove this point.

## ACKNOWLEDGMENT

## REFERENCES

1. Bertini, I., Luchinat, C., Maret, W., and Zeppezauer, A. (1986) *Zinc Enzymes*, Vol. 1, Birkhauser Boston, Inc., Cambridge, MA.
2. Wilkinson, G. (1987) *Comprehansive Coordination Chemistry: The Synthesis, Reactiones, Properties and Applications of Coordination Compounds*, Vol. 5, Pergamon Press, London.
3. Peretz, M., Bogin, O., Keinan, E., and Burstein, Y. (1993) *Int. J. Pept. Protein Res. 42*, 490−595.
4. Bogin, O., Peretz, M., Hacham, Y., Korkhin, Y., Frolow, F., Kalb, A. J., and Burstein, Y. (1998) *Protein Sci. 7*, 1156−1163.
5. Peretz, M., and Burstein, Y. (1989) *Biochemistry 28*, 6549−6555.
6. Zhang, Z., Djebli, A., Shoham, M., Frolow, F., Peretz, M., and Burstein, Y. (1993) *J. Mol. Biol. 230*, 353−355.
7. Korkhin, Y., Frolow, F., Bogin, O., Peretz, M., Kalb, A. J., and Burstein, Y. (1996) *Acta Crystallogr., Sect. D 52*, 882−886.
8. Korkhin, Y., Kalb (Gilboa), A. J., Peretz, M., Bogin, O., Burstein, Y., and Frolow, F. (1998) *J. Mol. Biol. 278*, 967−981.
9. Ford, B. J., Askins, K. J., and Taylor, K. B. (1993) *Biotechnol. Bioeng. 42*, 367−375.

10. Oestreicher, E. G., Pereira, D. A., and Pinto, G. F. (1996) *J. Biotechnol. 46*, 23−31.

11. Pereira, D. A., Pinto, G. F., and Oestreicher, E. G. (1994) *J. Biotechnol. 34*, 43−50.

12. Eklund, H., Plapp, B. V., Samama, J. P., and Branden, C. I. (1982) *J. Biol. Chem. 257*, 14349−14358.

13. Al-Karadaghi, S., Cedergren-Zeppezauer, E. S., and Hovmoller, S. (1994) *Acta Crystallogr., Sect. D 50*, 793−807.

14. Perlman, L., and Wolff, J. (1968) *Science 160*, 317−319.

15. Eklund, H., and Branden, C. (1978) *J. Biochem. 254*, 3458−3461.

16. Peretz, M., Weiner, L. M., and Burstein, Y. (1997) *Protein Sci 6*, 1074−1083.

17. Bogin, O., Peretz, M., and Burstein, Y. (1997) *Protein Sci. 6*, 450−458.

18. Stern, E. A., Newville, M., Ravel, B., Yacoby, Y., and Haskel, D. (1995) *Physica B 208−209*, 117−128.

19. Korkhin, Y., Kalb, A. J., Peretz, M., Bogin, O., Burstein, Y., and Frolow, F. (1998) *J. Mol. Biol. 278*, 967−981.

20. Zabinsky, S. I., Rehr, J. J., Ankudinov, A., Albers, R. C., and Eller, M. J. (1995) *Phys. Rev. B 52*, 2995−2999.

21. Rehr, J. J., de leon Mustre, J., Zabinsky, S. I., and Albers, R. C. (1991) *J. Am. Chem. Soc. 113*, 5135−5138.

22. Chadha, V. K., Leidal, K. G., and Plapp, B. V. (1983) *J. Med. Chem. 26*, 916−922.

23. Binsted, N., Strange, R. W., and Hasnain, S. S. (1992) *Biochemistry 31*, 12117−12125.

24. Chance, R. M., Miller, L. M., Fischetti, R. F., Scheuring, E., Huang, W., Sclavi, B., Hai, Y., and Sullivan, M. (1996) *Biochemistry 35*, 9014−9023.

25. Scott, R. A. (1985) *Methods Enzymol. 117*, 414−458.

26. Sagi, I., Hochman, Y., Bunker, G. S., and Carmeli, C. (1995) in *Proceedings of the Xth International Photosynthesis Congress*, Kluwer, Dordrecht, The Netherlands.

27. Sagi, I., Hochman, Y., Bunker, G., Carmeli, S., and Carmeli, C. (1998) *J. Synchrotron Radiat. 98*, 788−791.

28. Sagi, I., Hochman, Y., and Carmeli, C. (1997) *Photosynth. J. 56*, 547−551.

29. Sagi, I., Hochman, Y., and Carmeli, C. (1998) *Photosynth. Res. 57*, 1−11.

30. Durham, P. J. (1988) *Theory of XANES*, Vol. 92, Wiley, Interscience Publication, Eindhoven, The Netherlands.

31. Wirt, M. D., Sagi, I., Chen, E., Frisbie, S., and Chance, R. M. (1990) *J. Am. Chem. Soc. 112*, 5299.

32. Stern, E. A. (1993) *Phys. Rev. B 48*, 9825.

33. Woody, R. W. (1995) *Methods Enzymol. 246*, 34−71.

34. Strickland, E. H. (1974) *CRC Crit. Rev. Biochem. 2*, 113−175.

35. Eklund, H., Nordstrom, B., Zeppezauer, E., Soderlund, G., Ohlsson, I., Boiwe, T., Soderberg, B. O., Tapia, O., Branden, C. I., and Akeson, A. (1976) *J. Mol. Biol. 102*, 27−59.

36. Ramaswamy, S., el Ahmad, M., Danielsson, O., Jornvall, H., and Eklund, H. (1996) *Protein Sci. 5*, 663−671.

37. Eftink, M. R. (1991) *Methods Biochem. Anal. 35*, 127−205.

38. Eklund, H., and Branden, C. I. (1979) *J. Biol. Chem. 254*, 3458−3461.

39. Eklund, H., Samma, J. P., Wallen, L., Branden, C. I., Akeson, A., and Jones, T. A. (1981) *J. Mol. Biol. 146*, 561−587.

40. Eklund, H., Nordstrom, B., Zeppezauer, E., Soderlund, G., Ohollsen, I., Boiwe, T., and Branden, C. I. (1974) *FEBS Lett. 44* (1), 200−204.

41. Dworschak, R. T., and Plapp, B. V. (1977) *Biochemistry 16*, 2716−2725.

42. Dunn, M. F. (1975) *Struct. Bonding (Berlin) 23*, 61.

43. Morris, R. G., Saliman, G., and Dunn, M. F. (1980) *Biochemistry 19*, 725−731.

44. Makinen, M. W., Maret, W., and Yim, M. B. (1983) *Arch. Biochem. Biophys. 223*, 213−223.

45. Li, C., Heatwole, J., Soelaiman, S., and Shoham, M. (1999) *Proteins: Struct., Funct., Genet. 37*, 619−627.

46. Colby, T. D., Bahnson, B. J., Chin, J. K., Klinman, J. P., and Goldstein, B. M. (1998) *Biochemistry 37*, 9295−9304.

47. Cha, Y., Murray, C. J., and Klinman, J. P. (1989) *Science 243*, 1325−1330.

48. Iweibo, I., and Weiner, H. (1972) *Biochemistry 11*, 1003−1009.

49. Deng, H., Schindler, J. F., Berst, K. B., Plapp, B. V., and Callender, R. (1998) *Biochemistry 37*, 14267−14278.

50. Rulisek, L., and Vondrasek, J. (1998) *J. Inorg. Biochem. 1*, 1−14.

51. Alberts, I. L., Nadassy, K., and Wodak, S. J. (1998) *Protein Sci. 7*, 1700−1716.